Dynamic adult tracheal plasticity drives stem cell adaptation to changes in intestinal homeostasis.

Jessica Perochon[1], Gabriel N. Aughey[2], Tony D. Southall[2] and Julia B. Cordero[1*].

[1] Institute of Cancer Sciences-University of Glasgow, Wolfson Wohl Cancer Research Centre Garscube Estate, Switchback Road, Glasgow, G61 1QH

[2] Department of Life Sciences, Imperial College London, London, SW7 2AZ.

*Corresponding author: julia.cordero@glasgow.ac.uk

Tight coordination of stem cell function by local and systemic signals is essential to preserve adult tissue homeostasis and organismal health. The vasculature is a prominent component of various stem cell niches [1-5]. However, its role in intestinal homeostasis is largely unknown. Here, we uncover a previously unrecognised crosstalk between intestinal stem cells (ISCs) of the adult *Drosophila* midgut and the vasculature-like tracheal system[6], which is essential for regeneration of the injured intestine. Following local damage to the intestinal epithelium, gut-derived reactive oxygen species (ROS) and FGF ligand lead to reversible remodelling of gut-associated terminal tracheal cells through HIF-1α/FGFR signaling activation. Reciprocally, the provision of oxygen and FGF by the trachea drive ISC proliferation following damage. Strikingly, we find that adult tracheal plasticity involves downregulation of key developmental tracheal specification genes and upregulation of the highly conserved pro-neuronal remodelling IGF2 mRNA-binding protein (IGF2BP2/Imp). Altogether, our results reveal a novel intestinal/vasculature inter-organ communication program, which is essential to adapt stem cells' response to the proliferative demands of the intestinal epithelium.

26 The *Drosophila* tracheal system is an oxygen-delivering interconnected tubular
27 network, functionally analogous to the mammalian vascular and respiratory systems[6].
28 Following specification from epidermal cells and the formation of a tracheal sac in the embryo,
29 tracheal cells undergo extensive cell rearrangements and cell shape changes leading to the
30 formation of multicellular tubes that ramify into progressively thinner branches, culminating
31 with a terminal tracheal cell[6]. Terminal tracheal cells (TTCs) extend prominent cytoplasmic
32 projections, which supply oxygen to surrounding tissues[6-8]. Mimicking the highly vascular
33 nature of the mammalian intestine, the adult *Drosophila melanogaster* midgut is extensively
34 covered by TTCs labelled with a *GAL4* reporter driven under the control of the *Drosophila*
35 homologue of Serum Response Factor (dSRF)[9] (*dSRF>GFP*) (Fig.1a). Transmission electron
36 microscopy of posterior midguts denoted intimate contact between TTCs, enterocytes (ECs)
37 (Fig.1b) and ISCs (Fig.1c). Oxygen and nutrient availability are two recognised determinants
38 of TTC plasticity[10, 11]. However, we noticed that local damage to the adult *Drosophila* intestinal
39 epithelium caused by ingestion of the pathogenic bacteria *Pseudomonas entomophila* (*Pe*),
40 the DNA-damaging agent Bleomycin or the pro-inflammatory agent Dextran Sulfate Sodium
41 (DSS) caused a significant increase in TTC coverage within the posterior midgut, which was
42 most noticeable in areas displaying high ISC proliferation (Fig.1d, e and Extended data Fig.1a,
43 b). Similarly, damage to the mouse intestinal epithelium induced by whole body irradiation
44 revealed a significant increase of $CD31^{+ve}$ endothelial cells in areas surrounding the
45 regenerating crypts (Fig.1f), suggesting a conserved nature of damage-induced
46 vasculature/tracheal plasticity in the intestine. Importantly, increased TTC coverage of the
47 *Drosophila* midgut upon damage is independent of gut resizing (Extended Data Fig.1c-e) and
48 does not involve TTC proliferation (Fig.1g and Extended Data Fig.1f). Collectively, these data
49 suggest an extensive cellular remodelling of TTCs in response to intestinal epithelial injury.
50 This is further supported by the increased number of secondary and tertiary tracheal branches
51 and total tracheal length in individual TTCs (Fig.1h-j). A time course assessment of posterior
52 midguts over a 16 hrs period of oral bacterial infection (Damage phase) followed by 32 hrs of
53 normal diet feeding (Recovery phase) revealed direct correlation between tracheal coverage

54 and ISC proliferation (Fig.1k, l and Extended Data Fig.1g, h). These results strongly suggest
55 that the observed adult gut-associated-tracheal remodelling is a highly dynamic and reversible
56 process that accompanies changes in intestinal homeostasis.

57 We next asked whether tracheal cells had a functional role in the regeneration of the
58 midgut following damage, which is characterised by a robust increase in ISC proliferation[12-14]
59 (Fig.1d). To address this question, we ablated TTC in the adult by expressing the pro-apoptotic
60 gene *bax* (*UAS-bax*) using a temperature sensitive *dSRF-Gal4* (*dSRF*^{ts}: *dSRF-Gal4*; *tubulin-*
61 *gal80*^{ts}) (Fig.2a, b). Adult TTC ablation led to a significantly impaired regenerative response of
62 the intestine to multiple damages, with an approximate 50% decrease in ISC proliferation
63 (Fig.2c). Therefore, TTCs are required to achieve full levels of ISC proliferation during
64 regeneration of the adult midgut following damage. TTCs are best known for their role
65 facilitating gas exchange with their target tissues[6]. Thus, poor intestinal regeneration following
66 tracheal ablation might be due to the lack of oxygen. To test this, we subjected animals to
67 high and prolonged hypoxic environmental conditions, which were effective to induce
68 expression of a transgenic reporter of *Drosophila* Hypoxia-inducible factor-1α (HIF-1α/Sima)
69 activity[15] (Extended Data Fig.2a, b) and TTC remodelling (Extended Data Fig.2a, c). We
70 observed that, while hypoxia clearly impaired damage induced ISC proliferation in the midgut
71 (Fig.2d), it did so by only 24% of the values observed in normoxia, which was significantly
72 lower than the 50% reduction observed upon TTC ablation (Fig.2c). This could be due to a
73 compensatory effect of the increased tracheal coverage induced by hypoxia (Extended Data
74 Fig.2a, c) or gut-associated trachea providing factors in addition to oxygen to the intestinal
75 epithelium[16].

76 Given that tracheal remodelling and ISC proliferation show almost the exact same
77 dynamics (Fig.1k, l), it is unclear whether these events are part of a feedforward mechanism
78 or if one precedes the other. To address this, we assessed tracheal remodelling following
79 damage while blocking ISC proliferation in the adult midgut by expressing a *UAS-myc RNAi*
80 (*myc-IR*)[17] using *escargot-GAL4; tubulin-gal80*^{ts} (*esg*^{ts}*>GFP*) (Fig.2e, f). As we need to use
81 the *GAL4/UAS* system to genetically manipulate gut cells, we established a scoring method

82 for assessing tracheal coverage through the use of light microscopy (Extended Data Fig.2d
83 and Methods). Our results show that gut-associated trachea was still able to remodel in *myc-*
84 *IR* midguts following *Pe* damage, in spite of the almost complete absence of ISC proliferation
85 (Fig.2f). Given that TTCs are necessary for ISC proliferation (Fig.2c), we conclude that
86 tracheal remodelling precedes midgut ISCs proliferation following damage. We therefore
87 hypothesise that signals activated by damage upstream of ISC proliferation might induce gut-
88 tracheal remodelling.

89 Epithelial stress caused by intestinal damage triggers a strong oxidative burst and
90 production of reactive oxygen species (ROS) within the midgut coming from enterocytes (ECs)
91 and ISCs/EBs[18, 19]. Thus, we hypothesise that ROS could be an important determinant of
92 tracheal remodelling in the regenerating intestine. Feeding animals with the antioxidant N-
93 acetyl cysteine (NAC) or genetically blocking ROS production in ECs by overexpressing the
94 enzyme *catalase*[18] using *NP1-GAL4; tubulin-gal80*^{ts} (*NP1*^{ts}*>GFP*) significantly impaired
95 damage-induced tracheal remodelling (Fig.2h, i and Extended Data Fig.2e, f) in addition to the
96 expected reduction in regenerative ISC proliferation (Fig. 2j and Extended Data Fig.2g)[18]. Of
97 note, the effect of NAC treatment on tracheal remodelling was stronger than what resulting
98 from blocking ROS production in ECs, which is consistent with the latter being only one of the
99 sources of ROS in the damaged midgut[19].

100 Exogenous H_2O_2 can stabilize HIF-1α —a key conserved driver of hypoxia-induced
101 tracheal/vascular remodelling[20-22]— in normoxia[23]. Remarkably, Sima/HIF-1α activity as per
102 the *ldh-lacZ* reporter was significantly increased within gut-associated TTCs following midgut
103 damage (Fig.2k, m). Conversely, *ldh-lacZ* became undetectable following NAC treatment
104 (Fig.2l, m). Altogether, these results suggest that ROS are important determinants of gut-
105 tracheal remodelling and HIF1-α/Sima pathway activation following intestinal damage. We
106 next assessed the functional role of HIF1-α/Sima in intestinal regeneration. Midguts from
107 *sima*$^{-/-}$ whole mutant animals or subject to adult specific *sima* knockdown (*sima-IR*) within
108 TTCs showed significantly impaired tracheal remodelling and ISC proliferation following
109 damage (Fig.3a-f). *Drosophila* fibroblast growth factor receptor (FGFR), Breathless (Btl), is a

110 well-known transcriptional target of HIF-1α[24, 25]. Consistently, a transgenic reporter of
111 *breathless (btl)* gene expression was significantly upregulated within TTCs in response to
112 intestinal damage (Fig.3g, h). TTC specific knockdown of *btl* using independent RNAi lines
113 (*btl-IR*) inhibited tracheal remodelling and ISC proliferation following damage (Fig.3i-k).
114 Therefore, activation of HIF-1α/FGFR signaling within TTCs following gut-damage is essential
115 for tracheal remodelling and regenerative ISC proliferation in the adult midgut.

116 During development or in hypoxia, the *FGF*-like ligand Branchless (Bnl) produced by
117 target tissues drives tracheal remodelling via FGFR/Breathless activation within the trachea[10,
118 26, 27]. Surprisingly, using a *bnl* reporter we observed that, while *bnl* was observed in a small
119 number of cells within the adult midgut following damage (Fig.4a), ligand expression was also
120 significantly upregulated in TTCs (Fig.4b-c). Consistently, qPCR from whole-midguts—
121 including gut-associated trachea— revealed up-regulation of *bnl* expression in damaged
122 *versus* control tissues (Fig.4d). We next used targeted RNAi knockdown to assess the
123 functional role of individual sources of FGF/Bnl in our system. Our results showed that, while
124 redundant for tracheal remodelling, *bnl* from TTCs is necessary for complete ISC proliferation
125 following damage of the adult midgut (Fig.4e-g). Complementary knockdown of the receptor
126 *btl* in ISCs/EBs strongly impaired ISC proliferation without affecting TTC remodelling upon
127 damage (Fig.4h-j), suggesting that ISC proliferation depends on intestinal Btl, partly activated
128 by Bnl from TTCs. We next assessed the functional role of gut derived Bnl. Individual ligand
129 knockdown in ISCs/EBs or ECs was sufficient to reduce ISC proliferation following damage
130 but did not impair tracheal remodelling (Extended Data Fig.4a-f). However, concomitant *bnl*
131 knockdown in ECs and ISCs/EBs resulted in significant impairment of both, ISC proliferation
132 and TTC remodelling (Fig.4k-m). Altogether, these results indicate that gut intrinsic
133 FGF/FGFR signaling can influence ISC proliferation in the gut, independently of TTCs
134 (Extended Data Fig.4a-f). Furthermore, consistent with the high sensitivity of the regenerative
135 intestine to small fluctuations in signaling activity[17, 28], thresholds of FGFR activity needed to
136 maintain complete ISC proliferation upon damage are higher than those required for full
137 tracheal remodelling. Hence, while sufficient to impact ISC proliferation, small variations in Bnl

138 amounts do not affect tracheal remodelling (Fig.4e-g and Extended data Fig.4a-f).
139 Consistently, knock down of multiple sources of gut-derived FGF/Bnl is needed to impact
140 tracheal FGFR/Btl signaling and subsequent TTC remodelling during intestinal regeneration
141 (Fig.4k-m). Importantly, we identify TTCs as an unexpected damage-inducible source of
142 FGF/Bnl, which contributes to FGFR/Btl activation within ISCs to induce their regenerative
143 proliferation (Fig.4, c, g).

144 We next used Targeted DamID (TaDa) for cell specific profiling of RNA Pol II chromatin
145 binding[29] to identify TTC intrinsic transcriptional changes following intestinal damage (Fig.5a).
146 TaDa is particularly advantageous in our system due to inherent difficulties to physically
147 separate tracheal tissue from the midgut. We identified 1747 genes significantly bound by
148 RNA Pol II in TTCs from control midguts (TableS2). Gene ontology (GO) analysis revealed an
149 overall enrichment in components of the tracheal system, and molecules involved in epithelial
150 tube morphogenesis, and respiratory/tracheal system development (Fig. 5b). We identified
151 359 genes upregulated, and 522 genes downregulated in TTCs, following midgut damage by
152 oral infection with *Pe* (Table S2). Consistent with our reporter expression data and functional
153 work (Fig.4b, c), this unbiased analysis identified *bnl/FGF* as a gene with significantly
154 increased RNA Pol II binding following *Pe* infection (TableS3) (Extended Data Fig.5a).
155 Interestingly, genes associated with neuronal differentiation and morphogenesis where
156 upregulated in TTCs following intestinal damage (Extended Data Fig.5b). Amongst the TTC
157 expressed genes with increased RNA Pol II binding upon gut damage, was the highly
158 conserved mRNA-binding protein Imp/IGF2BP (Fig.5c), which has been previously
159 characterised as a key regulator of axonal remodelling[30,31]. qRT-PCR confirmed *Imp*
160 upregulation in midgut and associated tracheal tissue upon damage (Extended Data Fig.5c).
161 Consistently, expression of two independent *Imp* RNAi lines (*Imp-IR*) within TTCs resulted in
162 significant impairment of tracheal remodelling and ISC proliferation following intestinal
163 epithelial damage (Fig.5d-f).

164 Unexpectedly, genes whose function is linked to epithelial tube morphogenesis and
165 respiratory tracheal system development appeared significantly decreased in TTCs following

166 midgut damage (Extended Data Fig.5d). *Trachealess* (*trh*) is expressed in all tracheal cells
167 from the onset of embryonic development through adulthood[25, 32, 33]. Loss of *trh* during
168 development prevents tracheal cell specification from precursor cells and tracheal tube
169 morphogenesis[32, 33]. However, in line with our GO term analysis of down-regulated genes
170 (Extended Data Fig.5d), *trh* and *ventral veinless* (*vvl*)— also required for tracheal
171 development[34]—displayed a strong decrease in RNA Pol II binding following gut damage
172 (Fig.5g and Extended Data Fig.5e) (Table S2). A transgenic reporter of *trh* expression (*trh-*
173 *lacZ*) was significantly downregulated in TTCs upon gut damage (Fig.5h, i). Remarkably, gene
174 reporter signal was restored following 32 hrs of damage removal (Fig.5h, i). Consistently, *trh*
175 overexpression in TTCs significantly impaired tracheal remodelling and ISC proliferation
176 during intestinal regeneration (Fig.5j-l). These results suggest that tracheal specification
177 genes need to be suppressed to allow gut-associated TTC plasticity and a robust intestinal
178 regenerative response in the adult.

179 As a determinant of tracheal specification, *trh* regulates multiple tracheal genes
180 including *btl*[32-34]. Indeed, TaDa indicates a suppression of RNA Pol II binding to *btl* in TTCs
181 following intestinal damage (Extended Data Fig.5f). However, our reporter data and functional
182 work show increased transcription and a positive role of *btl* during tracheal remodelling
183 following damage (Fig.3g-k), which is consistent with the role of Sima/ HIF-1α as an activator
184 of *btl* transcription[10] in the system (Fig.3a-f). Therefore, in the case of *btl*, RNA pol II occupancy
185 does not directly reflect on the gene transcriptional status at the time of our analysis. This
186 apparent discrepancy could be due to pausing of the polymerase or temporally dynamic *btl*
187 transcription influenced by low *trh* and increased Sima/ HIF-1α activity induced upon intestinal
188 damage, which may not be captured through TaDa.

189 Our results reveal a novel inter-organ communication program in *Drosophila,* involving
190 the adult tracheal system and the midgut, which drives reciprocal adaptation of both tissues
191 to sustain a robust regenerative response of the intestine to environmental challenges
192 (Fig.5m). Mechanistically, gut-derived ROS and FGF induce tracheal remodelling following
193 intestinal damage through paracrine activation of HIF-1α/FGFR signaling within TTCs.

Reciprocally, tracheal and gut FGF drives intestinal regeneration through FGFR signaling activation within ISCs. Furthermore, cell specific transcriptional profiling and genetic experiments show that adult TTC intrinsic changes conferring tracheal plasticity upon gut damage involve the activation of a neuronal growth-like program and suppression of tracheal cell fate. Our results may represent a general mechanism driving vasculature/stem cell interactions in the mammalian intestine and other self-renewing tissues.

217 **Methods**

218 **Fly stocks and rearing**. A complete list of fly stocks and full genotypes used in this study can
219 be found in Table S1. In experiments using *GAL4*/*GAL80*^{ts} flies were bred and F1s reared and
220 kept at 18°C for 5 days after eclosion. Animals were then transferred to 29°C for 3-5 days to
221 allow transgene activation prior to phenotypic analysis. Otherwise, crosses and offspring were
222 kept at 25°C. Animals of the desired phenotype were used in experiments after 10 days of
223 adult eclosion. Additional information on animal age is provided in each figure legend. Adult
224 flies were maintained in vials at low densities (10-15 flies per vial) and were transferred to
225 fresh food vials every 2 days. Only adult posterior midguts from mated females were analysed
226 in this study.

227

228 **Damage induced intestinal regeneration.** Oral administration of *Pe*, Bleomycin, DSS was
229 performed as previously described[12, 35, 36] with minor modifications. Briefly, 5-7-day-old female
230 flies of the desired genotypes were starved in empty vials for 2hrs followed by feeding with a
231 5% sucrose solution only (Sucrose), or containing either *Pe* at OD 100, 25□g/ml Bleomycin
232 (Sigma-Aldrich, Cat#B2434), or 3% DSS (Sigma-Aldrich, Cat#42867) applied on filter paper
233 discs (Whatman). *Pe* infection was carried out for 16hrs, Bleomycin feeding was done for 1-
234 day and DSS feeding lasted for 2-days with fresh media applied each day.

235

236 **NAC treatment.** Flies were placed in empty vials with a filter paper soaked with a 5% sucrose
237 solution containing 20mM NAC (Sigma-Aldrich, Cat#A7250) for 24hrs. Animals were then fed
238 with either 5% sucrose + NAC or 5% sucrose + NAC + *Pe* (OD 100) for an additional period
239 of 24hrs.

240

241 **Mouse intestinal regeneration and IHC.** Mice were subject to whole body 10 Gy gamma-
242 irradiation and the intestines were analysed 72h post-irradiation. Small intestines were
243 isolated and flushed with tap water. 10× 1cm portions of small intestine were bound together

244 with surgical tape and fixed in 4% neutral buffered formalin. Intestines from 3 mice per
245 condition were used. 4 μm sections of formalin–fixed paraffin–embedded (FFPE) tissues were
246 cut, mounted onto adhesive slides and incubated at 60°C overnight. Prior to staining, sections
247 were dewaxed for 5 minutes in xylene followed by rehydration through decreasing
248 concentrations of alcohol and final washing with H2O for 5 minutes. FFPE sections underwent
249 heat–induced epitope retrieval in a Dako pre-treatment module. Sections were heated in
250 Target Retrieval Solution High pH (Dako, K8004) for 20 minutes at 97°C before cooling to
251 65°C. Slides were removed and washed in Tris Buffered Saline with Tween (TbT) (Dako,
252 K8000) and loaded onto a Dako autostainer link48 platform where they were stained with anti-
253 CD31 antibody 1:75 (Abcam, ab28364) following standard IHC procedures. All animal work
254 has been approved by a University of Glasgow internal ethics committee and performed in
255 accordance with institutional guidelines under personal and project licenses granted by the
256 UK Home Office (PPL PCD3046BA).
257
258 **Hypoxic treatment.** Adult flies were grown at 25°C or 29°C in 21% O_2 (Normoxia) at a density
259 of 15-20 flies per vial. Then, animals were transferred overnight to 3% O_2 (Hypoxia) in a
260 Whitley Scientific H35 hypoxystation incubator.
261
262 ***Drosophila* immunohistochemistry.** Immunohistochemistry was carried out as described
263 previously[17]. The following antibodies were used: chicken anti-GFP 1:200 (Abcam, ab13970),
264 mouse anti-PH3 1:100 (Cell Signaling, 9706), rabbit anti-□gal 1:1000 (MP Biochemicals
265 #559761), rabbit anti-DsRed 1:1000 (Clontech, #632496), CBP 1:100 gift from Marta
266 Llimargas. Alexa Fluor 488, 546 and 647 (Invitrogen) were used for secondary antibodies at
267 1:200 and 1:100 respectively. Guts were mounted in Vectashield anti-fade mounting medium
268 for fluorescence with DAPI (Vector Laboratories, Inc) to visualize all nuclei.
269
270

271 **Image acquisition.**

272 *Transmission Electron Microscopy*. Guts were dissected under Schneider's insect medium
273 and were subsequently fixed in 2.5% glutaraldehyde in 0.1 M cacodylate buffer (pH 7.4) for
274 1hr RT. Samples were rinsed repeatedly in 0.1M sodium cacodylate buffer, before post fixation
275 treatment in 1% Osmium Tetroxide/buffer for 1hr and washing with dH20 for 30mins. Samples
276 were then stained in 0.5% Uranyl Acetate/dH20 for 1hr (in dark) and dehydrated by incubation
277 in a graded series of Ethanol. Samples were subject to three subsequent incubations in
278 Propylene Oxide followed by Epon 812 resin/ Propylene Oxide (50:50) mix and left on a rotator
279 overnight, followed by several incubations in pure Epon resin. Samples were then embedded
280 into blocks and oven incubated at 60°C for 48hrs. Ultrathin sections (50-70nm thickness) were
281 cut using a Leica Ultracut UCT. The sections produced were collected on Formvar coated 100
282 mesh copper grids and subsequently contrast stained in 2% Methanolic Uranyl Acetate for
283 5mins followed by Reynolds Lead Citrate for 5mins. Gut samples were viewed using a JEOL
284 1200 EX TEM and Images captured using a Cantega 2K x 2K camera and Olympus ITEM
285 Software.

286 *Confocal microscopy Zeiss LSM 780*. Each image represents half-volume of the full posterior
287 midgut (area comprised between hindgut and Copper Cell Region) and were acquired with
288 20x or 40x oil immersion lenses using identical acquisition conditions for all samples from a
289 given experiment. Images were collected using Zen 2012 SP1 Release version 8.1 software.
290 Images represent maximal intensity projection of a stable number of Z-Stacks and were
291 processed with ImageJ to adjust brightness and contrast.

292 *Light microscopy Axio observer Zeiss*. Adult guts were dissected in PBS, mounted in 100%
293 glycerol and image immediately. Up to three pictures per posterior midgut were taken to cover
294 most of the area. Images were taken at their most apical plane to best detect TTCs with a 20x
295 lens. Images were collected using Zen 2 software. Mouse intestines (Fig. 1f) were acquired
296 using this microscope with a 20x lens.

297

298 **Quantifications in the adult posterior midgut.**

299 *Quantification of ISC proliferation*. Antibodies against Phosphorylated Histone H3 (PH3) were
300 used to detect ISC proliferation in the posterior midgut. Total number of $PH3^{+ve}$ cells per
301 posterior midgut was quantified using an Olympus BX51 microscope. Number of midguts
302 analysed (n) for each experiment are indicated in the figures.

303 *Quantification of tracheal coverage from immunofluorescence images*. Confocal images of
304 *dSRF>GFP* expressing midguts were used. Full posterior midguts were individually processed
305 on ImageJ as follows: 1) maximum projection Z stacks were produced; 2) area of interest was
306 cropped to eliminate Malpighian tubules, hindgut and copper cell region; 3) "threshold" was
307 adjusted for ensuring the detection of most terminal tracheal branches; 4) function
308 "skeletonize" was applied to generate a skeleton of the tracheal network; 5) the mean intensity
309 of this skeleton was measured. Number of midguts analysed (n) for each experiment are
310 indicated in the figures.

311 *Quantification of tracheal branching form light-microscopy images*. Acquired images were
312 blindly scored using a 1 to 5 scaling system (Extended Data Fig.2d). The custom ImageJ
313 macro used for tracheal blind scoring is available at
314 https://github.com/emltwc/TracheaProject/blob/master/Blind_scoring.ijm. Number of midguts
315 analysed (n) for each experiment are indicated in the figures.

316 *Quantification of number of TTC ramifications*. Maximum intensity projection from confocal
317 imaging Z stacks were used. The number of primary, secondary and tertiary branches derived
318 from a single TTC body was assessed. Levels of tracheal branching were assigned as
319 indicated in Fig.1h. Number of TTC analysed (n) and midguts analysed for each condition are
320 indicated in the corresponding figure and figure legend.

321 *Quantification total tracheal length*. We used the plugin "NeuronJ" from ImageJ to quantify the
322 total length of all the branches emerging from a single TTC. maximum projection Z stacks.
323 Number of TTC analysed (n) and midguts analysed for each condition is indicated in the
324 corresponding figure and figure legend.

325 *Quantification of TTC nuclei*. Confocal images of posterior midguts from animals expressing
326 *dSRF>RedStinger* to label TTC nuclei were used. The custom ImageJ macro used for
327 quantifying the number of TTC nuclei is available at
328 https://github.com/emltwc/TracheaProject/blob/master/dSrf_pH3_overlap_for%20Jessica.ijm
329 . Number of midguts analysed (n) for each condition is indicated in the corresponding figure.

330 *Quantification of posterior midgut area*. Midgut tissue was visualized by Dapi staining and the
331 posterior midgut area (length x width) was measured with ImageJ. Number of midguts
332 analysed (n) for each condition is indicated in the corresponding figure.

333 *Quantification of lacZ reporters*. Antibodies against □-galactosidase were used to detect
334 *lactate dehydrogenase-*, *breathless-*, *branchless-* and *trachealess-lacZ* reporters. Pictures
335 were taken with confocal microscopy and staining was quantified using ImageJ. The mean
336 intensity of the gut area without staining was subtracted from the total □-galactosidase signal
337 mean intensity detected in TTCs. The difference was then divided by the mean intensity of the
338 gut area without staining to normalize data. Number of TTC analysed (n) and midguts
339 analysed for each condition is indicated in the figures.

340 **Statistical analysis.** Graph Pad Prism 6 version 6.07 software was used for statistical
341 analyses. Information on sample size and statistical tests used for each experiment are
342 indicated in the figure legends. All experiments represent a minimun of 2 independent
343 biological replicates. Measurements were taken from distinct samples.

344

345 **qRT-PCR.**

346 Trizol (Invitrogen) was used to extract total RNA from 30 midguts per biological replicate.
347 cDNA synthesis was performed using the High-Capacity cDNA Reverse Transcription Kit
348 (Applied Biosystems). QuantiNova SYBR Green (Qiagen) was used for qPCR. Data were
349 extracted and analysed using QuantStudio and Prism 6.0. Data from 3 biological replicates
350 are presented as the mean fold change with standard error.

351 Primers used for qRT-PCR were:

352 Rpl32_F TGCCCACCGGATTCAAGAAG

353 Rpl32_R TCGACAATCTCCTTGCGCTT

354 bnl_F CAAGTTCCGAGGCCCAAGG

355 bnl_R TGGGGATCTTGGTTGCACTG

356 Imp_F GGTGGGCCGTATCATTGG [37]

357 Imp_R TCACGCGCTGCAATTCC [37]

358 **Targeted DamID (TaDa), library preparation, sequencing and data analysis.** *dSRF-*
359 *GAL4*^{ts} flies were crossed with to *UAS-LT3-DAM* or *UAS-LT3-Dam-Pol II* flies at 18°C.
360 Progeny were collected every 48hrs and aged for a further 7 days at 18°C before transferring
361 to 29°C to induce Dam protein expression for 24hrs. During the last 16hrs at 29°C, flies were
362 fed on Sucrose only or on Sucrose + *Pe* solution. 60 midguts per condition were dissected in
363 cold PBS and stored at -80°C. Methylated DNA fragments were isolated and next generation
364 sequencing libraries were prepared as described previously[38]. Sequencing data from TaDa
365 experiments were processed using a previously described pipeline[39] and mapped to release
366 6.03 of the *Drosophila* genome. Transcribed genes were annotated for Pol II binding data
367 using a custom Perl script[38] (available at https://github.com/tonysouthall/Dam-
368 RNA_POLII_analysis) using release 6.11 of the annotated *Drosophila* genome. Transcribed
369 genes were identified based on meeting a threshold of 1% FDR and > 0.2 log2 ratios. To
370 define differentially Pol II bound genes, log2 ratios for each GATC fragment were subtracted
371 to produce comparison files on which the same analysis was repeated. Significantly Pol II
372 bound genes appearing in both original and comparison files were selected to distinguish from
373 false positives arising from the presence of negative log2 values in the data. Gene Ontology
374 (GO) term analysis was performed using the R package ClusterProfiler[40] to search for
375 enriched GO terms in each condition.

376

377

378

379

380 **Data availability**.

381 Sequencing data related to Figure 5 are available through the Universtiy of Glasgow
382 institutional repositories *DOI: 10.5525/gla.researchdata.994 (2020)*. The entire set of raw data
383 supporting this study will be made accessible through the same repository prior to publication.

384

385 **Acknowledgements.**

386 We are thankful to Marta Llimargas, Markus Affolter, Irene Miguel-Aliaga, Andrea Brand,
387 Cedric Polesello, Pablo Wappner and Ilan Davis for generously sharing reagents and fly lines.
388 We thank the Kyoto, Vienna and Bloomington Drosophila Stock Centres and the Drosophila
389 Studies Hybridoma Bank for fly stocks and antibodies. We thank Colin Nixon (Beatson CRUK
390 histology service) for IHC of mouse intestinal samples, Elaine McKenzie for help with the use
391 of the hypoxia chamber, Margaret Mullin for assistance with TEM and David Strachan, John
392 Halpin and Robert Insall (Beatson CRUK) for support with image quantification. We thank
393 David McGuinness and Julie Galbraith (Glasgow Polyomics) for sequencing samples for TaDa
394 and Rhoda Stefanatos and Yachuan Yu for assistance with RT-qPCRs. We thank past and
395 present members of the Cordero lab. In particular, Maté Naszai for help with the creation of
396 custom ImageJ macros and Lynsey Carroll for providing mouse intestinal samples. We thank
397 Jean-Philippe Parvy and multiple members of the Cordero lab for scientific discussion and
398 advice on the project. J.P. and J.B.C. are funded by a Wellcome Trust and Royal Society Sir
399 Henry Dale Fellowship (Grant Number 104103/Z/14/Z) and a Wellcome Trust Institutional
400 Strategic Support Fund (ISSF) — Excellence and Innovation Catalyst Award to J.B.C. J.P.
401 was partly funded by a BBSRC - Flexible Talent Mobility Account (FTMA) Award
402 (BB/R506576/1). T.D.S and G.N.A. were funded by a Wellcome Trust Investigator grant
403 (104567; T.D.S.) and a BBSRC grant (BB/P017924/1; T.D.S. and G.N.A.)

404 **Author contributions.**

405 J.P designed and carried out all the experiments and analysed and interpreted the data.
406 Writing – original draft: J.P. G.A and T.S analysed the TaDa data. J.B.C conceived the project,

designed experiments, analysed the data and supervised the study. J.P and J.B.C wrote the paper.

410 **References.**

411 1. Mohyeldin, A., Garzon-Muvdi, T. & Quinones-Hinojosa, A. Oxygen in stem cell biology:
412 a critical component of the stem cell niche. *Cell Stem Cell* **7**, 150-161 (2010).
413 2. Rafii, S., Butler, J.M. & Ding, B.S. Angiocrine functions of organ-specific endothelial
414 cells. *Nature* **529**, 316-325 (2016).
415 3. Gur-Cohen, S. *et al.* Stem cell-driven lymphatic remodeling coordinates tissue
416 regeneration. *Science* **366**, 1218-1225 (2019).
417 4. Li, K.N. *et al.* Skin vasculature and hair follicle cross-talking associated with stem cell
418 activation and tissue homeostasis. *Elife* **8** (2019).
419 5. Sanchez Bosch, P. *et al.* Adult Drosophila Lack Hematopoiesis but Rely on a Blood
420 Cell Reservoir at the Respiratory Epithelia to Relay Infection Signals to Surrounding
421 Tissues. *Dev Cell* **51**, 787-803 e785 (2019).
422 6. Ghabrial, A., Luschnig, S., Metzstein, M.M. & Krasnow, M.A. Branching
423 morphogenesis of the Drosophila tracheal system. *Annu Rev Cell Dev Biol* **19**, 623-
424 647 (2003).
425 7. Affolter, M. *et al.* Tube or not tube: remodeling epithelial tissues by branching
426 morphogenesis. *Dev Cell* **4**, 11-18 (2003).
427 8. Cela, C. & Llimargas, M. Egfr is essential for maintaining epithelial integrity during
428 tracheal remodelling in Drosophila. *Development* **133**, 3115-3125 (2006).
429 9. Gervais, L. & Casanova, J. The Drosophila homologue of SRF acts as a boosting
430 mechanism to sustain FGF-induced terminal branching in the tracheal system.
431 *Development* **138**, 1269-1274 (2011).
432 10. Centanin, L. *et al.* Cell autonomy of HIF effects in Drosophila: tracheal cells sense
433 hypoxia and induce terminal branch sprouting. *Dev Cell* **14**, 547-558 (2008).
434 11. Linneweber, G.A. *et al.* Neuronal control of metabolism through nutrient-dependent
435 modulation of tracheal branching. *Cell* **156**, 69-83 (2014).

436 12. Amcheslavsky, A., Jiang, J. & Ip, Y.T. Tissue damage-induced intestinal stem cell
437 division in Drosophila. *Cell Stem Cell* **4**, 49-61 (2009).
438 13. Buchon, N., Broderick, N.A., Chakrabarti, S. & Lemaitre, B. Invasive and indigenous
439 microbiota impact intestinal stem cell activity through multiple pathways in Drosophila.
440 *Genes Dev* **23**, 2333-2344 (2009).
441 14. Chatterjee, M. & Ip, Y.T. Pathogenic stimulation of intestinal stem cell response in
442 Drosophila. *J Cell Physiol* **220**, 664-671 (2009).
443 15. Lavista-Llanos, S. *et al.* Control of the hypoxic response in Drosophila melanogaster
444 by the basic helix-loop-helix PAS protein similar. *Mol Cell Biol* **22**, 6842-6853 (2002).
445 16. Li, H., Qi, Y. & Jasper, H. Dpp signaling determines regional stem cell identity in the
446 regenerating adult Drosophila gastrointestinal tract. *Cell Rep* **4**, 10-18 (2013).
447 17. Cordero, J.B., Stefanatos, R.K., Scopelliti, A., Vidal, M. & Sansom, O.J. Inducible
448 progenitor-derived Wingless regulates adult midgut regeneration in Drosophila. *EMBO*
449 *J* **31**, 3901-3917 (2012).
450 18. Ha, E.M. *et al.* An antioxidant system required for host protection against gut infection
451 in Drosophila. *Dev Cell* **8**, 125-132 (2005).
452 19. Hochmuth, C.E., Biteau, B., Bohmann, D. & Jasper, H. Redox regulation by Keap1 and
453 Nrf2 controls intestinal stem cell proliferation in Drosophila. *Cell Stem Cell* **8**, 188-199
454 (2011).
455 20. Centanin, L., Gorr, T.A. & Wappner, P. Tracheal remodelling in response to hypoxia.
456 *J Insect Physiol* **56**, 447-454 (2010).
457 21. Rey, S. & Semenza, G.L. Hypoxia-inducible factor-1-dependent mechanisms of
458 vascularization and vascular remodelling. *Cardiovasc Res* **86**, 236-242 (2010).
459 22. Bacon, N.C. *et al.* Regulation of the Drosophila bHLH-PAS protein Sima by hypoxia:
460 functional evidence for homology with mammalian HIF-1 alpha. *Biochem Biophys Res*
461 *Commun* **249**, 811-816 (1998).

462 23. Chandel, N.S. *et al.* Reactive oxygen species generated at mitochondrial complex III
463 stabilize hypoxia-inducible factor-1alpha during hypoxia: a mechanism of O2 sensing.
464 *J Biol Chem* **275**, 25130-25138 (2000).
465 24. Ohshiro, T. & Saigo, K. Transcriptional regulation of breathless FGF receptor gene by
466 binding of TRACHEALESS/dARNT heterodimers to three central midline elements in
467 Drosophila developing trachea. *Development* **124**, 3975-3986 (1997).
468 25. Chung, S., Chavez, C. & Andrew, D.J. Trachealess (Trh) regulates all tracheal genes
469 during Drosophila embryogenesis. *Dev Biol* **360**, 160-172 (2011).
470 26. Sutherland, D., Samakovlis, C. & Krasnow, M.A. branchless encodes a Drosophila
471 FGF homolog that controls tracheal cell migration and the pattern of branching. *Cell*
472 **87**, 1091-1101 (1996).
473 27. Du, L. *et al.* Unique patterns of organization and migration of FGF-expressing cells
474 during Drosophila morphogenesis. *Dev Biol* **427**, 35-48 (2017).
475 28. Johansson, J. *et al.* RAL GTPases Drive Intestinal Stem Cell Function and
476 Regeneration through Internalization of WNT Signalosomes. *Cell Stem Cell* **24**, 592-
477 607 e597 (2019).
478 29. Marshall, O.J., Southall, T.D., Cheetham, S.W. & Brand, A.H. Cell-type-specific
479 profiling of protein-DNA interactions without cell isolation using targeted DamID with
480 next-generation sequencing. *Nat Protoc* **11**, 1586-1598 (2016).
481 30. Medioni, C., Ramialison, M., Ephrussi, A. & Besse, F. Imp promotes axonal remodeling
482 by regulating profilin mRNA during brain development. *Curr Biol* **24**, 793-800 (2014).
483 31. Samuels, T.J., Jarvelin, A.I., Ish-Horowicz, D. & Davis, I. Imp/IGF2BP levels modulate
484 individual neural stem cell growth and division through myc mRNA stability. *Elife* **9**
485 (2020).
486 32. Isaac, D.D. & Andrew, D.J. Tubulogenesis in Drosophila: a requirement for the
487 trachealess gene product. *Genes Dev* **10**, 103-117 (1996).
488 33. Wilk, R., Weizman, I. & Shilo, B.Z. trachealess encodes a bHLH-PAS protein that is an
489 inducer of tracheal cell fates in Drosophila. *Genes Dev* **10**, 93-102 (1996).

490 34. Anderson, M.G. *et al.* Function of the Drosophila POU domain transcription factor
491 drifter as an upstream regulator of breathless receptor tyrosine kinase expression in
492 developing trachea. *Development* **122**, 4169-4178 (1996).
493 35. Buchon, N., Broderick, N.A., Poidevin, M., Pradervand, S. & Lemaitre, B. Drosophila
494 intestinal response to bacterial infection: activation of host defense and stem cell
495 proliferation. *Cell Host Microbe* **5**, 200-211 (2009).
496 36. Myant, K.B. *et al.* Rac1 drives intestinal stem cell proliferation and regeneration. *Cell*
497 *Cycle* **12**, 2973-2977 (2013).
498 37. Toledano, H., D'Alterio, C., Czech, B., Levine, E. & Jones, D.L. The let-7-Imp axis
499 regulates ageing of the Drosophila testis stem-cell niche. *Nature* **485**, 605-610 (2012).
500 38. Southall, T.D. *et al.* Cell-type-specific profiling of gene expression and chromatin
501 binding without cell isolation: assaying RNA Pol II occupancy in neural stem cells. *Dev*
502 *Cell* **26**, 101-112 (2013).
503 39. Marshall, O.J. & Brand, A.H. damidseq_pipeline: an automated pipeline for processing
504 DamID sequencing datasets. *Bioinformatics* **31**, 3371-3373 (2015).
505 40. Yu, G., Wang, L.G., Han, Y. & He, Q.Y. clusterProfiler: an R package for comparing
506 biological themes among gene clusters. *OMICS* **16**, 284-287 (2012).

507

508

509

510

511

512

513

514 **Fig. 1 – Adult terminal tracheal cell plasticity in response to intestinal injury**. **a**,
515 Representative confocal image of terminal tracheal cells (TTCs) (green) surrounding the adult
516 digestive tract of *Drosophila*. Scale bar, 500□m. **b**, **c**, Transmission electron microscopy of a
517 posterior midgut cross-section highlighting the close interaction between a TTC (green pseudo
518 coloured) and an enterocyte (EC) (b) or an intestinal stem cell (ISC) (c; red pseudo coloured),
519 VM: visceral muscle, Scale bars, 5□m. **d**, Confocal images of TTC coverage (green) and ISC
520 proliferation (PH3; red) in control (Sucrose) or damaged (*Pe* infected) adult posterior midguts.
521 Dotted boxes in left panels indicate the area showed magnified in the right panels. Scale bars:
522 100□m in main figure and 50□m in close up view. **e,** Quantification of tracheal coverage in
523 posterior midguts as in (d) and from animals treated with Bleomycin or DSS as in (Extended
524 Data Fig.1b). Statistics: Student's t test; n= number of posterior midguts quantified; error bars
525 ± SEM. **f**, Immunohistochemical analysis of gut associated vasculature in control and
526 regenerating small mouse intestines using anti-CD31 endothelial cell antibody. Nuclei are
527 stained in blue with Hematoxylin. Scale bars: 100□m in main figure and 50□m in close up
528 view. **g,** Quantification of the number of TTC nuclei in posterior midguts from control or *Pe*
529 infected adult posterior midguts. Statistics: Student's t test; n= number of posterior midguts
530 quantified; error bars ± SEM. **h**, Representative confocal image of one terminal tracheal body
531 cell and its pseudo coloured primary (I^R), secondary (II^R) and tertiary (III^R) branches. Scale
532 bar, 50□m. **i**, Quantification of number of branches per TTC from control or *Pe* infected adult
533 posterior midguts. Statistics: Two-way ANOVA followed by Sidak's multiple comparisons test;
534 n= number of TTC quantified from 6 posterior midguts per condition; error bars ±SEM. **j**,
535 Quantification of total tracheal length per TTC (see Methods). Student's t test; n= number of
536 TTCs quantified from 6 posterior midguts per condition; error bars ± SEM. **k**, **l**, Quantification
537 of tracheal coverage and $PH3^+$ ISCs in posterior midguts during a 16 hrs period of *Pe* induced
538 intestinal damage followed by 32 hrs incubation in standard food. Statistics: Student's t test
539 was used to compare each timepoint within the damage and recovery stage against the 0 hrs
540 and 16 hrs, respectively. n= number posterior midgut quantified; error bars ±SEM. Where
541 indicated, *$p < 0.05$, **$p < 0.01$, ***$p < 0.001$ ****$p< 0.0001$. See also Extended Data Fig.1.

542

543 **Extended data Fig. 1 – Characterization and quantification of tracheal remodelling**
544 **following intestinal damage. a**, Representative confocal image of adult TTCs (green)
545 associated to a posterior midgut. Illustration of the different steps followed for the quantification
546 of gut tracheal coverage as explained in Methods. Scale bar, 100□m. Box in top panel
547 highlights the area shown in the bottom panels **b,** Representative confocal images of TTCs
548 (green) associated to posterior midguts from control animals (Suc) or animals fed with
549 Bleomycin or DSS. Scale bar, 50□m. **c**, Representative confocal images of control (Suc) or
550 damaged (*Pe*) adult posterior midguts (orange). Scale bar, 100□m. **d**, **e**, Quantification of
551 posterior midgut area (d) and ratio of tracheal coverage over adult posterior midgut area (e).
552 Statistics: Student's t test; n= number of posterior midguts quantified; error bars ±SEM. ****p<
553 0.0001. **f**, Confocal images of adult TTCs (green) from control (Suc) or *Pe* damaged posterior
554 midguts stained with anti-PH3 to label proliferating ISCs (red). Bottom panels represent
555 orthogonal views of the midguts shown in the top panels. Scale bar, 50□m. **g**, Confocal images
556 of adult TTCs assessed at the indicated time points during and after intestinal damage. White
557 lines trace an individual TTCs in each time point and condition. Scale bar, 50□m. **h**,
558 Correlation graph between TTCs gut coverage and ISC proliferation for each of the time points
559 and conditions presented in (g). Statistics: Pearson's correlation coefficient (r)=0.9660 and
560 0.9962; **p=0.0075 and 0.0038 in damage and recovery phases, respectively.

561

562 **Fig. 2 – Tracheal remodelling induced by midgut-derived ROS upon damage is required**
563 **for intestinal regeneration. a**, Confocal images of adult posterior midgut from control animals
564 or upon adult-specific *bax*-driven TTC ablation (green). Scale bar, 100□m. **b**, Quantification
565 of tracheal coverage in posterior midguts as in (a). Statistics: Student's t test; n= number of
566 posterior midguts quantified; error bars ±SEM. **c-d**, Quantification of $PH3^+$ ISCs in posterior
567 midguts of the genotypes and conditions indicated. Statistics: Two-way ANOVA followed by
568 Sidak's multiple comparisons test; n= number of posterior midguts quantified; error bars

569 ±SEM. **e**, Representative brightfield images of adult posterior midguts from Sucrose fed and
570 *Pe* infected animals without (control) or with adult-specific expression of *myc* RNAi within
571 ISCs/EBs (*esg*^{ts}>). Scale bar, 50□m. **f**, **g**, Quantification of PH3^{+} ISCs (f) and blindly scored
572 tracheal branching (g) in posterior midguts of genotypes and conditions as in (e). Statistics:
573 Two-way ANOVA followed by Sidak's multiple comparisons test; n= number of posterior
574 midguts quantified, error bars ±SEM. **h**, Representative confocal images of control and *Pe*
575 treated adult posterior midguts in the presence or absence of the antioxidant NAC. Scale bar,
576 100□m. **i**, **j**, Quantification of tracheal coverage (i) and PH3^{+} ISCs (j) in posterior midguts in
577 (h). Two-way ANOVA followed by Sidak's multiple comparisons test; n= number of posterior
578 midguts quantified; error bars ±SEM. **k**,**l,** Confocal images of the HIF-1α /Sima activity reporter
579 *ldh-lacZ* (grey) in control or *Pe* infected adult posterior midguts without or with NAC (k, l ,
580 respectively). Scale bar, 50□m. **m**, Quantification of the average *ldh-lacZ* staining intensity in
581 TTC within a defined region of the posterior midgut as in (k, l). Statistics: Two-way ANOVA
582 followed by Sidak's multiple comparisons test; n= number of TTC quantified from 9 to 10
583 posterior midguts/condition; error bars ±SEM. Where indicated, *p < 0.05, **p < 0.01, ***p <
584 0.001 ****p< 0.0001. See also Extended Data Fig.2.

585

586 **Extended data Fig. 2 – Gut associated TTCs are responsive to environmental oxygen**
587 **levels and gut produced ROS. a,** Representative confocal images of HIF-1α/Sima activity
588 reporter *ldh-lacZ* (grey) in adult posterior midguts from animals in normoxia (21% O_2) or
589 subjected to 24 hrs of hypoxia (3% O_2). Scale bar, 50□m. **b**, Quantification of the average *ldh-*
590 *lacZ* staining intensity within TTC in posterior midguts as in (a). Statistics: Student's t test; n=
591 number of TTC quantified from 9 posterior midguts/condition; error bars ±SEM. **c**,
592 Quantification of tracheal coverage in adult posterior midgut as in (a). Statistics: Student's t
593 test; n= number of posterior midguts quantified; error bars ±SEM. **d**, Examples of tracheal
594 branching levels assigned to each of the scores used for blind scoring of tracheal coverage
595 from light microscopy images. **e**, Representative brightfield images from control (Suc) or *Pe*

596 damaged posterior midguts from wild type animals or upon adult-specific *catalase*
597 overexpression within ECs. Scale bar, 50□m. **e**, **f**, Blind scoring of tracheal branching (f) and
598 quantification of PH3 $^{+}$ ISCs (g) in posterior midguts as in (e). Statistics: Two-way ANOVA
599 followed by Sidak's multiple comparisons test; n= number of posterior midguts quantified, error
600 bars ±SEM. Where indicated, *p < 0.05, **p < 0.01, ***p < 0.001 ****p< 0.0001.

601

602 **Fig. 3 – Activation of HIF-1α/FGFR signaling in TTCs is required for tracheal remodelling**
603 **and intestinal regeneration following damage. a,** Representative confocal images of
604 control (Sucrose) or *Pe* infected adult posterior midguts from wild type or *Sima*$^{-/-}$ whole mutant
605 animals. Scale bar, 100□m. **b**, **c**, Quantification of tracheal coverage (b) and PH3 $^{+}$ ISCs (c)
606 in posterior midguts as in (a). Statistics: Two-way ANOVA followed by Sidak's multiple
607 comparisons test; n= number of posterior midguts quantified, error bars ±SEM. **d**, Confocal
608 images of control (Sucrose) or *Pe* infected adult posterior midguts from wild type animals or
609 animals subject to adult-specific *sima* RNAi overexpression (*sima-IR*) within TTC
610 (*dSRF*^{ts}*>GFP*). Scale bar, 100□m. **e**, **f**, Quantification of tracheal coverage (e) and PH3 $^{+}$ ISCs
611 in posterior midguts as in (d). Statistics: Two-way ANOVA followed by Sidak's multiple
612 comparisons test; n= number of posterior midguts quantified, error bars ± SEM. **g**,
613 Representative confocal images of a *btl* expression reporter *btl-lacZ* (grey) in control (Sucrose)
614 and damaged (*Pe*) adult posterior midguts. Scale bar, 50□m. **h**, Quantification of the average
615 *btl-lacZ* staining intensity in TTC within a defined region of posterior midguts as in (g).
616 Statistics: Student's t test; n= number of TTC quantified from 5 to 7 posterior midguts/
617 condition; error bars, ±SEM. **i**, Confocal images of control (Sucrose) and damaged (*Pe*) adult
618 posterior midguts from wild type animals or following *RNAi*-driven adult-specific *btl* knockdown
619 (*btl-IR*) within TTCs. Scale bar, 100□m. **j**, **k**, Quantification of tracheal coverage (j) and PH3 $^{+}$
620 ISCs in posterior midguts as in (i). Statistics: Two-way ANOVA followed by Sidak's multiple
621 comparisons test; n= number of posterior midguts quantified, error bars ±SEM. Where
622 indicated, *p < 0.05, **p < 0.01, ***p < 0.001 ****p< 0.0001.

623

624 **Fig. 4 – Reciprocal midgut/TTC activation of FGF/FGFR signaling drives tracheal**
625 **remodelling and ISC proliferation following intestinal damage. a, b,** Representative
626 confocal images of *FGF/bnl* expression reporter *bnl>GFPnlacZ* (green) in control (Sucrose)
627 and regenerating (*Pe*) adult posterior midguts stained with CBP (Chitin Binding Protein) to
628 visualise all tracheal tissue (magenta). Arrowheads indicate reporter signal within midgut cells.
629 Arrows indicate signal within TTC. Dotted boxes in panels in (b) indicate the area showed
630 magnified in the right panels. Scale bar, 50□m (a) and 100□m (b). **c**, Quantification of the
631 average *bnl>GFPnlacZ* staining intensity within TTCs in posterior midguts as in (b). Statistics:
632 Student's t test; n= number of TTC quantified from 12 posterior midguts/condition; error bars,
633 ±SEM. **d**, qRT-PCR for *bnl* from control (Sucrose) or *Pe* infected whole midguts, including
634 associated tracheal tissue. Data are represented as mean ± SEM. **e**, representative confocal
635 images of control (Sucrose) or regenerating (*Pe*) adult posterior midguts from wild type
636 animals or upon RNAi-driven adult-specific *bnl* knockdown (*bnl-IR*) within TTC. Scale bar,
637 50□m. **f**, **g**, Quantification of tracheal coverage (f) and PH3 $^{+}$ ISCs (g) in posterior midguts as
638 in (e). Statistics: Two-way ANOVA followed by Sidak's multiple comparisons test; n= number
639 of posterior midguts quantified, error bars ± SEM. **h**, representative brightfield images of
640 control (Sucrose) or regenerating (*Pe*) adult posterior midguts from wild type animals or upon
641 RNAi-driven adult-specific *btl* knockdown (*btl-IR*) within ISCs/EBs. Scale bar, 50□m. **i**, **j**,
642 Quantification of blindly scored tracheal branching (i) and PH3 $^{+}$ ISCs (j) in posterior midguts
643 as in (h). Statistics: Two-way ANOVA followed by Sidak's multiple comparisons test; n=
644 number of posterior midguts quantified, error bars ±SEM. **k**, Representative brightfield images
645 of control (Sucrose) or regenerating (*Pe*) adult posterior midguts from wild type animals or
646 upon RNAi-driven adult-specific *bnl* knockdown (*bnl-IR*) ISCs/EBs and ECs (*NP1>,*
647 *esg^{ts}>GFP*). Scale bar, 50□m. **l**, **m**, Quantification of blindly scored tracheal branching (l) and
648 PH3 $^{+}$ ISCs (m) in posterior midguts as in (k). Statistics: Two-way ANOVA followed by Sidak's
649 multiple comparisons test; n= number of posterior midguts quantified, error bars ± SEM.

650 Where indicated, *p < 0.05, **p < 0.01, ***p < 0.001 ****p< 0.0001. See also Extended Data
651 Fig.4.

652

653 **Extended data Fig. 4 – Individual sources of gut-derived Bnl are redundant for TTC**
654 **remodelling but required for damage induced ISC proliferation. a**, Representative
655 brightfield images from control (Suc) or *Pe* damaged posterior midguts from wild type animals
656 or following RNAi-driven adult-specific *bnl* knockdown (*bnl-IR*) within ISCs/EBs. Scale bar,
657 50□m. **b**, **c**, Quantification of blindly scored tracheal branching (b) and PH3 $^{+}$ ISCs (c) in
658 posterior midguts as in (a). Statistics: Two-way ANOVA followed by Sidak's multiple
659 comparisons test; n= number of posterior midguts quantified ± SEM. **d**, Representative
660 brightfield images from control (Suc) or *Pe* damaged posterior midguts from wild type animals
661 or upon adult-specific *bnl* knockdown (*bnl-IR*) within ECs. Scale bar, 50□m. **e**, **f**, Quantification
662 of blindly scored tracheal branching (e) and PH3 $^{+}$ ISCs (f) in posterior midguts as in (d).
663 Statistics: Two-way ANOVA followed by Sidak's multiple comparisons test; n= number of
664 posterior midguts quantified, error bars ± SEM. Where indicated, *p < 0.05, **p < 0.01, ***p <
665 0.001 ****p< 0.0001.

666

667 **Fig.5 – Transcriptional profiling of TTCs by targeted DamID revealed novel regulators**
668 **of tracheal remodelling and intestinal regeneration. a,** Schematic representation of TaDa
669 approach used to identify tracheal transcriptional programs responsive to intestinal damage.
670 **b**, Gene Ontology term analysis from control midguts (Sucrose). **c**, Profile of RNA Pol II
671 binding to *Imp* in TTCs from control (Suc) and regenerating (*Pe* damaged) midguts. Boxes
672 highlight areas with most prominent differences in RNA Pol binding. **d**, Representative
673 confocal images of control (Suc) or regenerating (*Pe*) adult posterior midguts from wild type
674 animals or upon RNAi-driven adult-specific *Imp* knockdown (*Imp-IR*) within TTCs (green).
675 Scale bar, 100□m. **e**, **f**, Quantification of tracheal coverage (e) and PH3 $^{+}$ ISCs (f) in posterior

676 midguts as in (d). Statistics: Two-way ANOVA followed by Sidak's multiple comparisons test;
677 n= number of posterior midguts quantified, error bars ±SEM. **g**, Profile of RNA Pol II binding
678 to *trh* within TTCs for control (Suc) and regenerating (*Pe*) midguts. **h**, Representative confocal
679 images of *trh* expression reporter *trh-lacZ* (grey) in control midguts (Sucrose), midguts after
680 16 hrs of *Pe* infection (damage), and midguts from animals returned to standard feeding
681 conditions for 32 hrs post-infection (recovery). Scale bar, 50□m. **i**, Quantification of the
682 average *trh-lacZ* staining intensity within TTCs within a defined compartment of posterior
683 midguts as in (h). Statistics: Student's t test; n= number of TTCs quantified from 4 to 11
684 posterior midguts/condition; error bars, ±SEM. **j**, Representative confocal images control (Suc)
685 or regenerating (*Pe*) adult posterior midguts from wild type animals or upon adult-specific *trh*
686 overexpression within TTCs (green). Scale bar, 100□m. **k**, **l**, Quantification of tracheal
687 coverage (k) and PH3 $^{+}$ ISCs (l) in posterior midguts as in (j). Statistics: Two-way ANOVA is
688 shown, followed by Sidak's multiple comparisons test; n= number of posterior midguts
689 quantified, error bars ±SEM. **m**, Working model. Where indicated, *p < 0.05, **p < 0.01, ***p
690 < 0.001 ****p< 0.0001. See also Extended Data Fig.5.

691

692 **Extended data Fig. 5 – Transcriptome profiling in TTC by targeted DamID**. **a**, RNA Pol II
693 binding profile to *bnl* in TTC from control (Suc) and damaged (*Pe*) adult midguts. **b**, Gene
694 Ontology term analysis of up-regulated genes. **c**, qRT-PCR for *Imp* from control (Suc) or *Pe*
695 infected whole midguts, including associated tracheal tissue. Data are represented as mean
696 ± SEM. **d**, Gene Ontology term analysis of down-regulated genes. **e**, **f**, RNA Pol II binding
697 profile to *vvl* and *btl* in TTC from control (Suc) and damaged (*Pe*) adult midguts.

698

Perochon, Figure 1

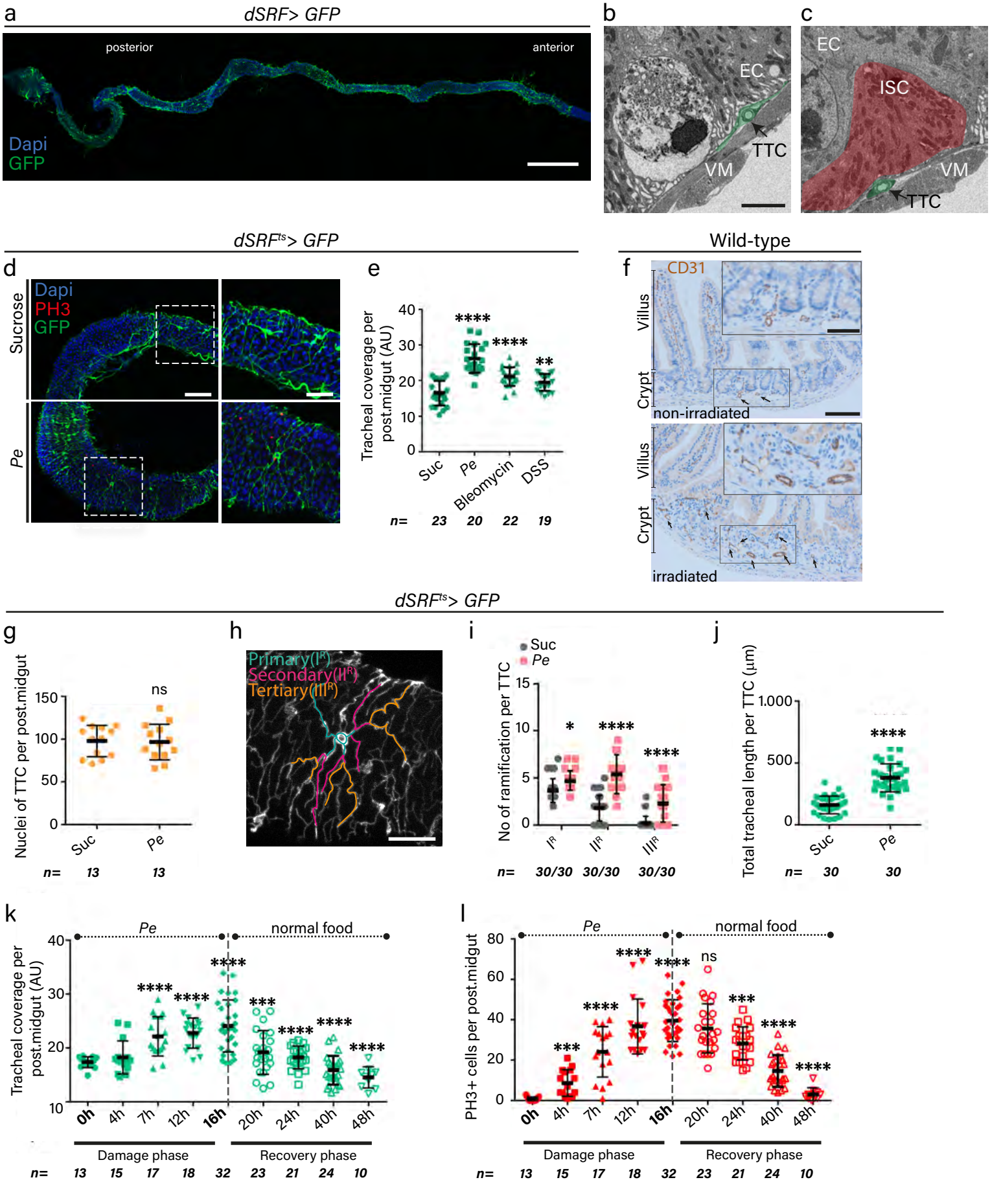

Perochon, Figure 2

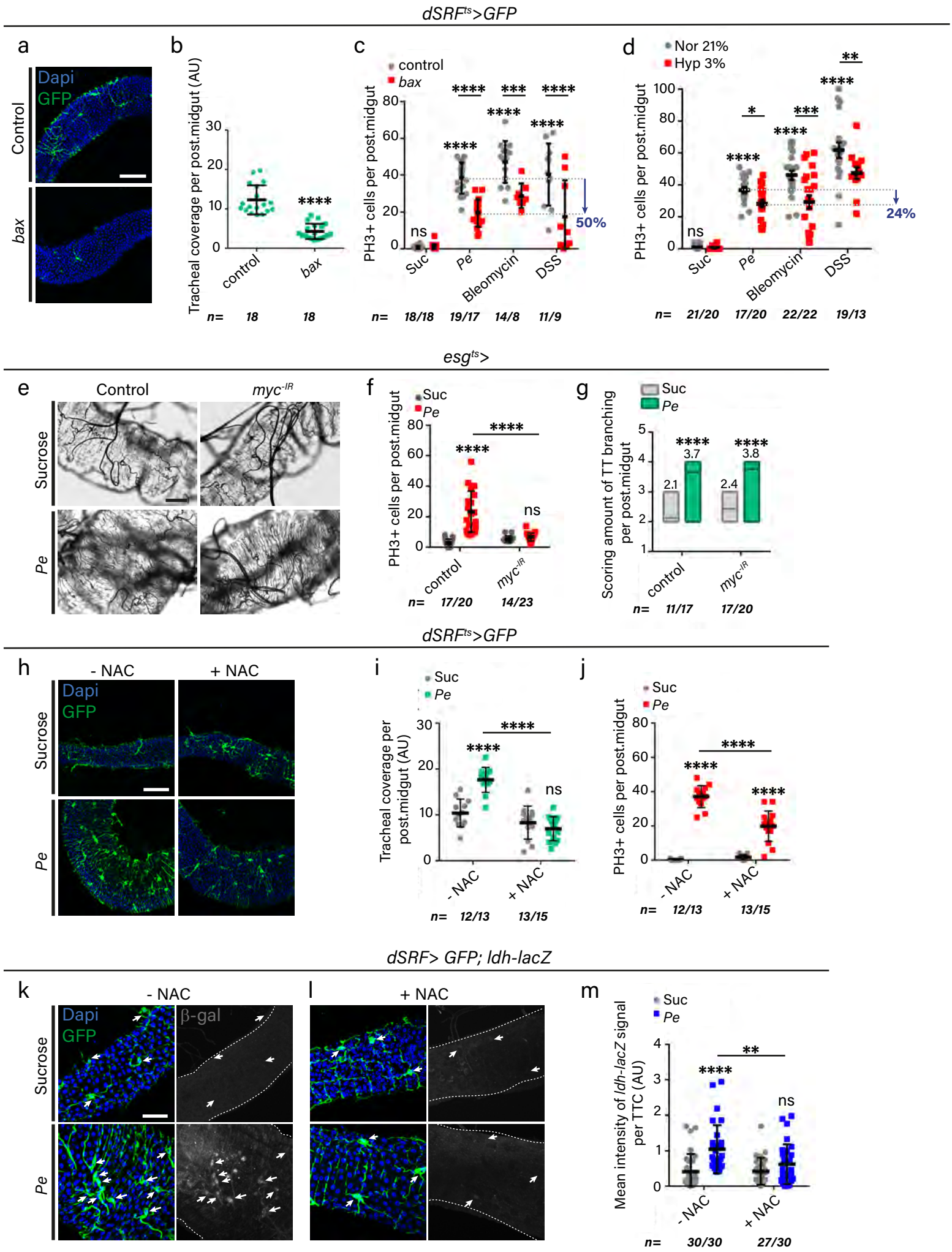

Perochon, Figure 3

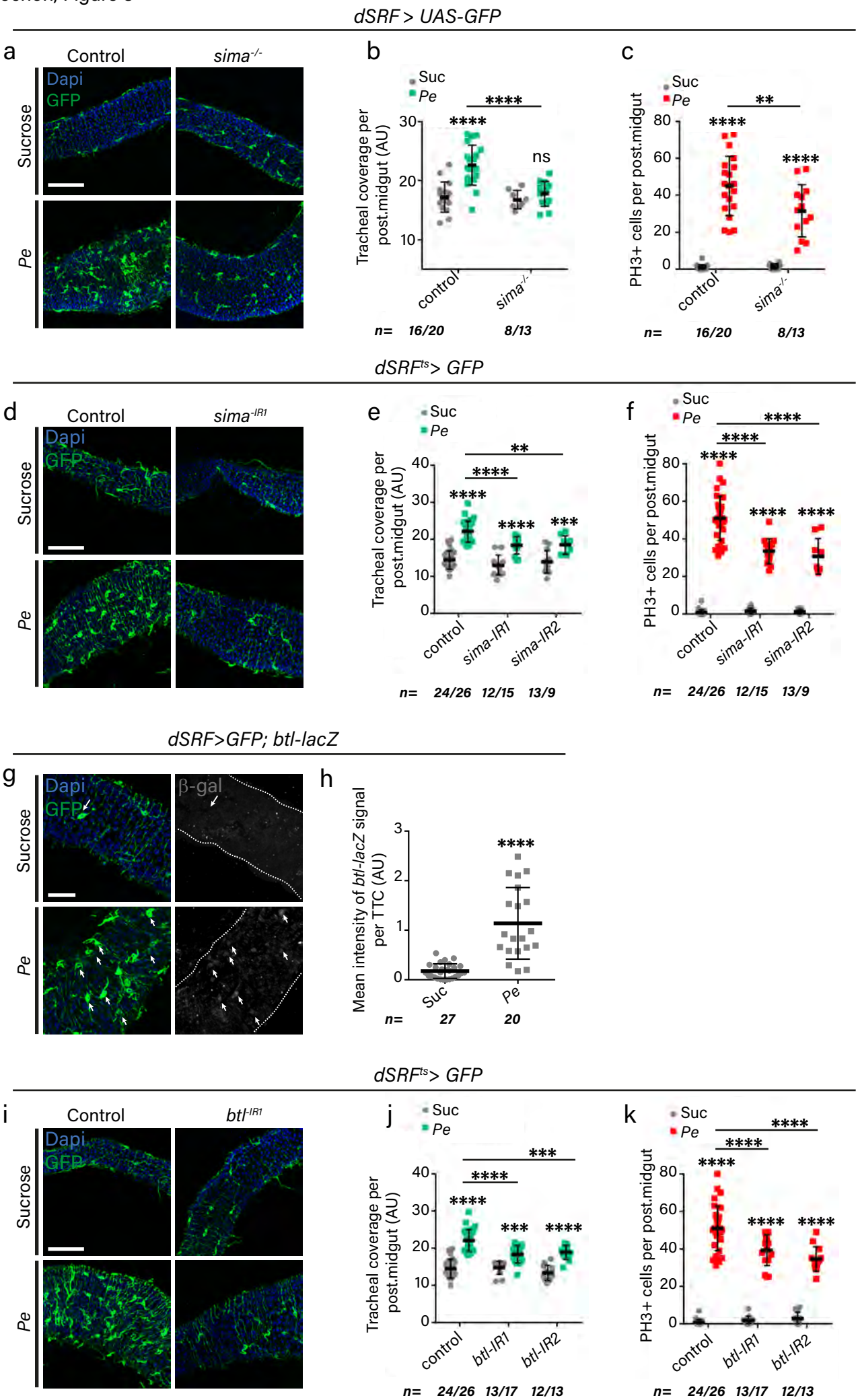

Perochon, Figure 4

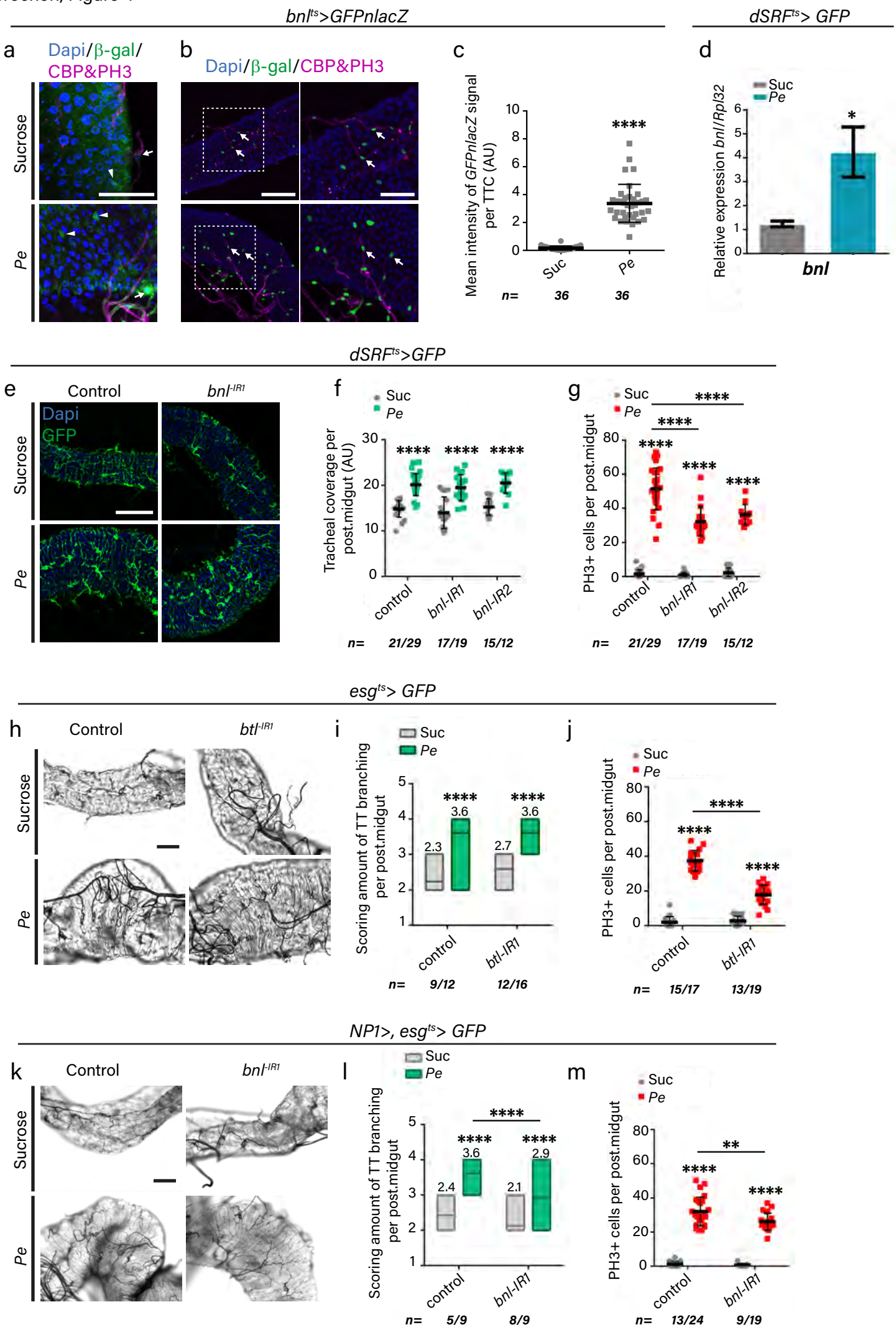

Perochon, Figure 5

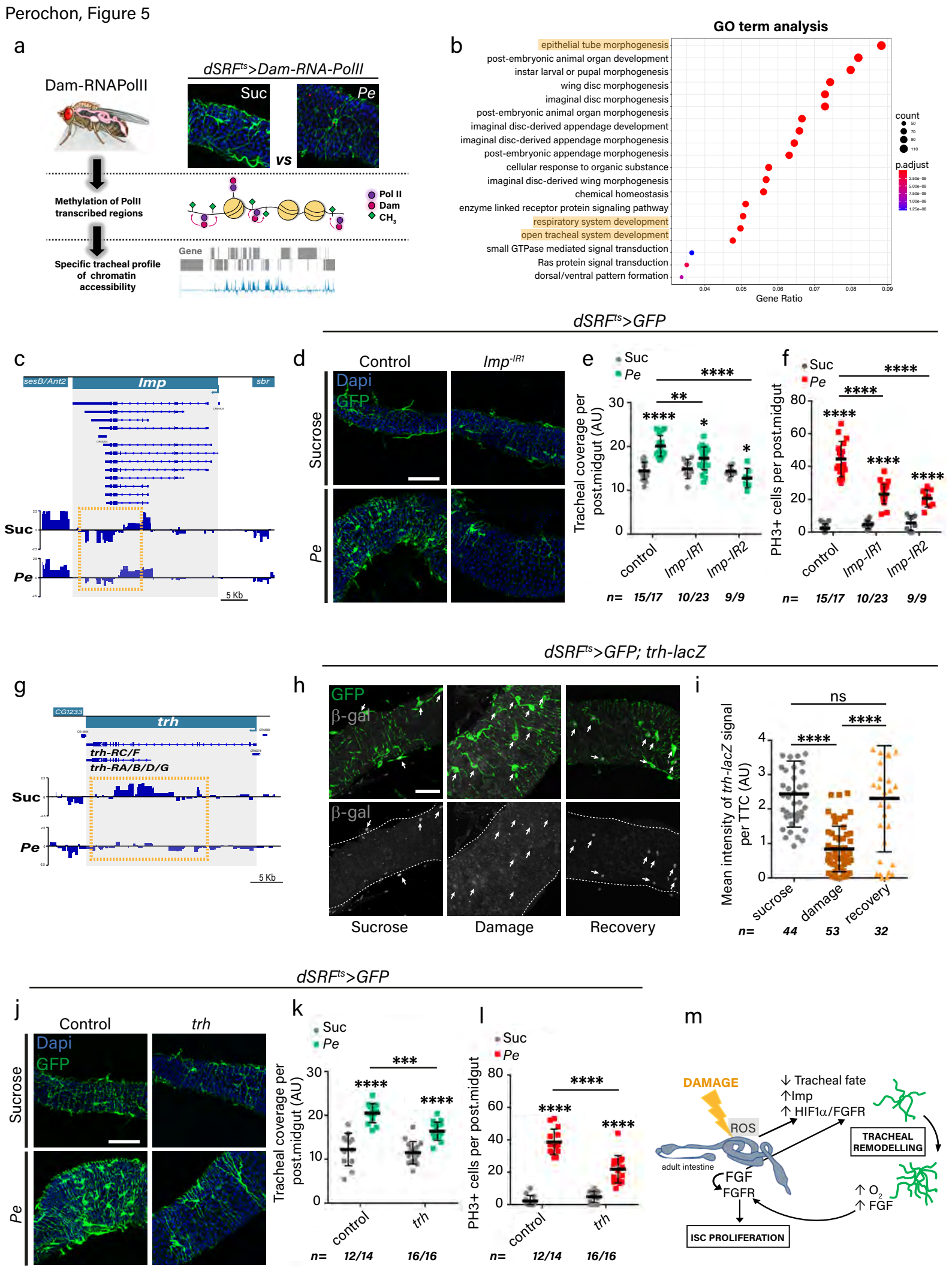

Perochon, Extended data Figure 1

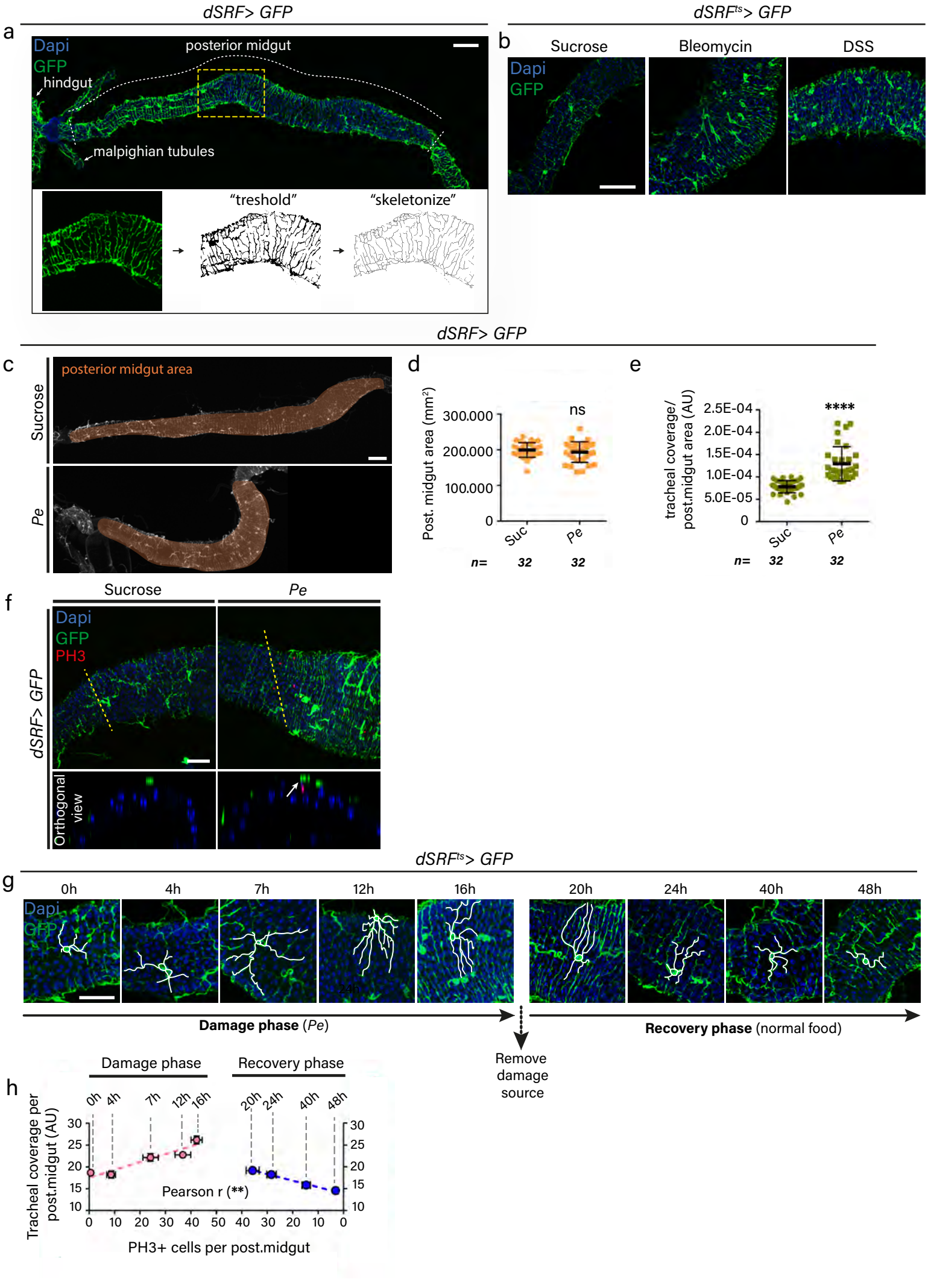

Perochon, Extended data Figure 2

dSRF > GFP; ldh-lacZ

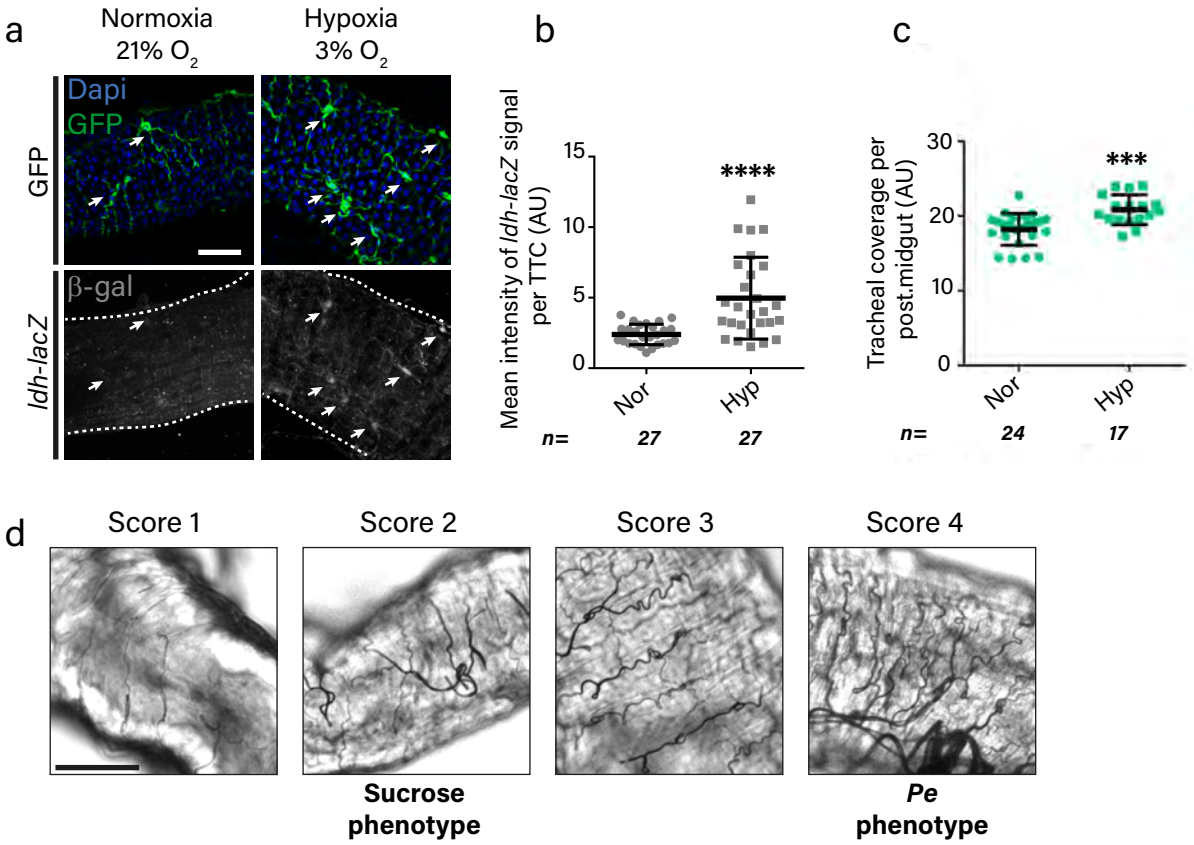

NP1ts > GFP

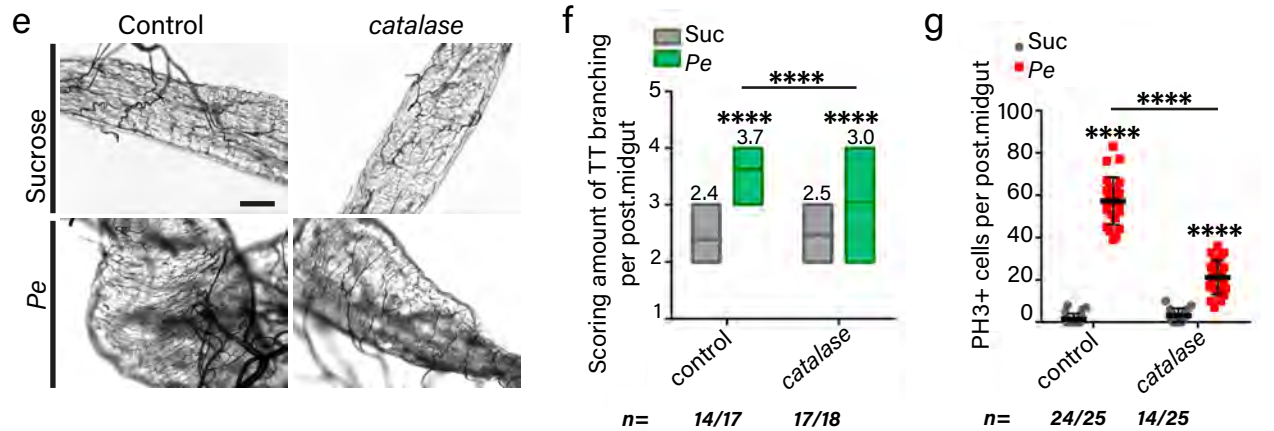

Perochon, Extended data Figure 4

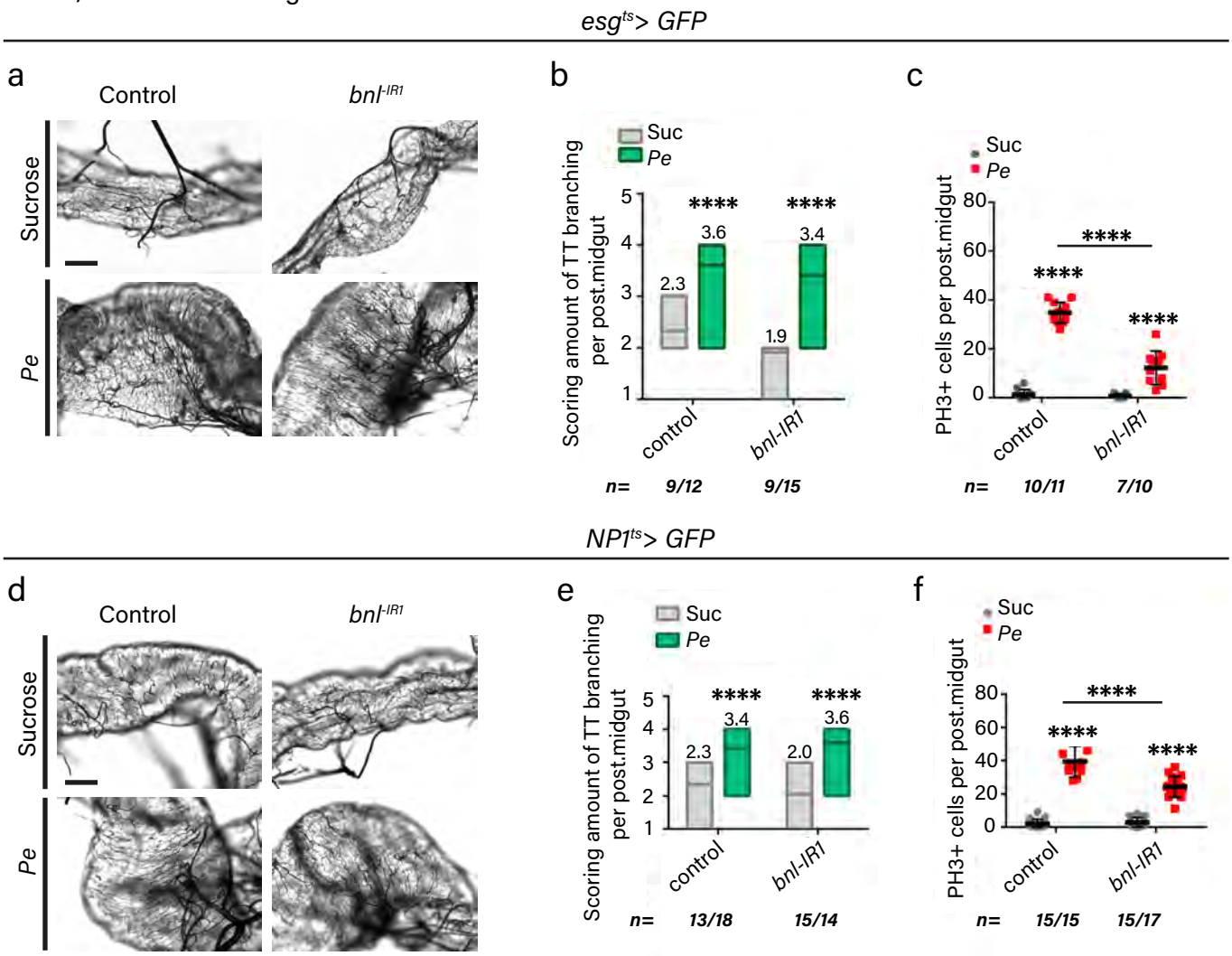
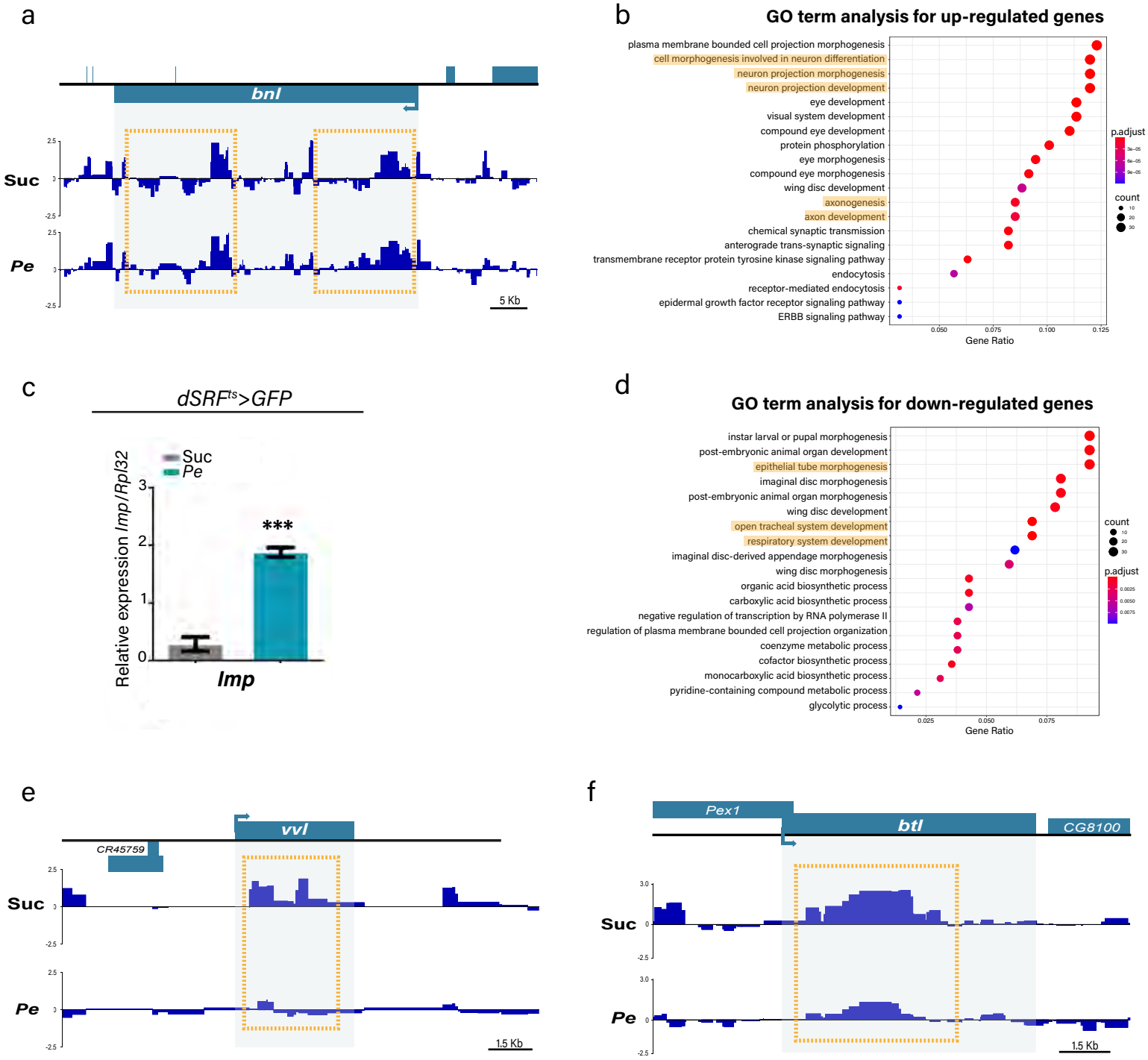
Perochon, Extended data Figure 5